PAPER

Cr$_2$O$_7{}^{2-}$ inside Zr/Hf-based metal–organic frameworks: highly sensitive and selective detection and crystallographic evidence†

Kun Wu, [ID] [a] Ji Zheng, [ID] [a] Yong-Liang Huang, [ID] [b] Dong Luo, [ID] [a] Yan Yan Li, [ID] [a] Weigang Lu [ID] *[a] and Dan Li [ID] *[a]

Herein, we report the synthesis of three pairs of isostructural zirconium- and hafnium-based homometallic metal–organic frameworks (MOFs, termed Zr-MOF-1 and Hf-MOF-1, Zr-MOF-2 and Hf-MOF-2, and Zr-MOF-3 and Hf-MOF-3) with respective **scu**, **sqc**, and **flu** topologies by using the aggregation-induced-emission (AIE) ligand H$_4$BTTB (4,4′,4″,4‴-(pyrazine-2,3,5,6-tetrayl)tetrabenzoic acid). As expected, all of them display excellent luminescence properties, and their potential application in the detection of Cr$_2$O$_7{}^{2-}$ has been extensively studied. Among them, Zr/Hf-MOF-2 exhibits the high adsorption capacity for Cr$_2$O$_7{}^{2-}$ (153 mg g^{-1} and 149 mg g^{-1}, respectively), while Zr/Hf-MOF-3 demonstrates exceptional sensitivity in the detection of Cr$_2$O$_7{}^{2-}$, and the limits of detection are calculated to be 0.013 μM and 0.019 μM, respectively. The values are comparable to those of the best-performing MOF materials reported so far. Significantly, single-crystal X-ray diffraction studies revealed the exact location and configuration of Cr$_2$O$_7{}^{2-}$ inside Zr/Hf-MOF-2. To the best of our knowledge, this is the first example of Zr/Hf-MOFs with direct evidence showing that Cr$_2$O$_7{}^{2-}$ is linked to the Zr/Hf oxide cluster by replacing its terminal H$_2$O/OH$^-$ groups within the single crystal.

1. Introduction

Nowadays, heavy metal pollution is not only causing severe environmental issues but also posing a huge health risk to humans.[1] Many heavy metals have been proven to be toxic and carcinogenic even at low concentrations. In addition, they are not biodegradable and often accumulate in biological systems.[2–7] Thus, the detection of trace heavy metals in water is particularly important for safeguarding public health.[8] Meanwhile, their presence as oxygenated ions may have a huge impact on waste-water treatment, leading to equipment scaling and corrosion.[9] Today, a variety of techniques have been applied for the removal of heavy metals in water, for example, photocatalytic reduction and degradation,[10] ion exchange,[11–14] and adsorption.[15,16] In general, adsorption with porous materials is regarded as an eco-friendly strategy because of multiple advantages such as large capacity and ease of operation.[17,18]

[a] College of Chemistry and Materials Science, and Guangdong Provincial Key Laboratory of Functional Supramolecular Coordination Materials and Applications, Jinan University, Guangzhou 510632, P. R. China. E-mail: weiganglu@jnu.edu.cn, danli@jnu.edu.cn

[b] Department of Chemistry, Shantou University Medical College, Shantou, Guangdong 515041, P. R. China

Chromium has been widely used in painting, electroplating, the leather industry and other related fields, and released into the environment in large quantities.[19,20] The United States Environmental Protection Agency (U.S. EPA) recommends that the concentration of hexavalent chromium (Cr(vi)), specifically in the form of dichromate Cr$_2$O$_7{}^{2-}$, in drinking water must be less than 100 ppb. Monitoring the Cr$_2$O$_7{}^{2-}$ content in water is thus important but turned out to be challenging. So far, various porous materials such as activated carbons, resins, zeolites, and other porous organic polymers have been explored for removing Cr$_2$O$_7{}^{2-}$.[21–23] However, their overall performance is less than satisfactory. Therefore, it is imperative and urgent to seek porous materials with high performance in the detection and removal of Cr$_2$O$_7{}^{2-}$ in water.

The adsorption of Cr$_2$O$_7{}^{2-}$ by ionic metal–organic frameworks (MOFs) is not always superior to that by neutral MOFs,[24,25] and thus matching pore size and strong interaction sites could be equally important. As newly emerged porous crystalline materials, MOFs are coordination polymers self-assembled by metal ions/clusters and organic bridging linkers.[26–31] In particular, through the modification of ligands, a variety of MOFs with different functions can be obtained. Their unprecedented porosity and tunable surface chemistry have made them promising materials for applications in gas storage/separation,[32,33] host–guest recognition,[34–41] light-harvesting,[42,43] absorption[44–47] and catalysis.[48,49] It should be pointed out that chemical stability

16974 | *J. Mater. Chem. C*, 2020, **8**, 16974–16983

This journal is © The Royal Society of Chemistry 2020

is a prerequisite for MOFs to be used in practical applications such as the removal of $Cr_2O_7^{2-}$ in water. Since the emergence of the first Zr-MOF (UiO-66) in 2008, a growing number of researchers have focused on the synthesis of Zr/Hf-based MOFs because of their excellent stability.[50] More interestingly, zirconium/hafnium oxide clusters exhibit strong affinity towards various oxygenated anions, including $Cr_2O_7^{2-}$, and Zr/Hf-MOFs have been frequently studied for the detection of $Cr_2O_7^{2-}$ in aqueous solutions.[51] In this work, we report a series of isomorphic Zr/Hf-MOFs (three isostructural pairs: Zr-MOF-1 and Hf-MOF-1, Zr-MOF-2 and Hf-MOF-2, and Zr-MOF-3 and Hf-MOF-3), featuring (4,8)-connected three-dimensional (3D) frameworks but with different topologies. They are constructed with an 8-connected Zr_6/Hf_6 node and the same X-shaped tetra-carboxylate organic linker in different conformations (Fig. 1 and Fig. S1, ESI†). The detection of $Cr_2O_7^{2-}$ in aqueous solutions has been extensively studied. Among them, Zr/Hf-MOF-2 with an **sqc** topology exhibits a high adsorption capacity for $Cr_2O_7^{2-}$ (153 mg g^{-1} and 149 mg g^{-1}, respectively), while the quenching constants of Zr/Hf-MOF-3, the one with a **flu** topology, are the highest (K_{sv} = 6.37 × 10^5 M^{-1} and 4.51 × 10^5 M^{-1}), and the detection limits were calculated to be 0.013 μM and 0.019 μM, respectively,

which are superior to those of many top-performing MOF materials in the detection of $Cr_2O_7^{2-}$. Significantly, single-crystal X-ray diffraction studies revealed the exact location and configuration of $Cr_2O_7^{2-}$ inside Zr/Hf-MOF-2. To the best of our knowledge, this is the first example of Zr/Hf-MOFs with direct evidence showing that $Cr_2O_7^{2-}$ is linked to the Zr/Hf oxide cluster by replacing its terminal H_2O/OH^- groups within the single crystal.

2. Experimental

2.1 Materials and instruments

All reagents were of analytical grade and used without further purification. The ligand 4,4′,4″,4‴-(benzene-1,2,4,5-tetrayl)-tetrabenzoic acid (H$_4$BTTB) was synthesized according to a method reported in the literature (Scheme S1 and Fig. S3–S8, ESI†).[52] Elemental analyses of C, H, and N were carried out on an Elementar Vario Micro cube CHNS analyzer. Powder X-ray diffraction (PXRD) was performed on a Rigaku Ultima IV diffractometer (Cu Kα radiation, λ = 1.5406 Å). Single-crystal X-ray diffraction (SCXRD) data were collected at 100 K *via* an Oxford Cryo stream system on an XtaLAB PRO MM007-DW diffractometer
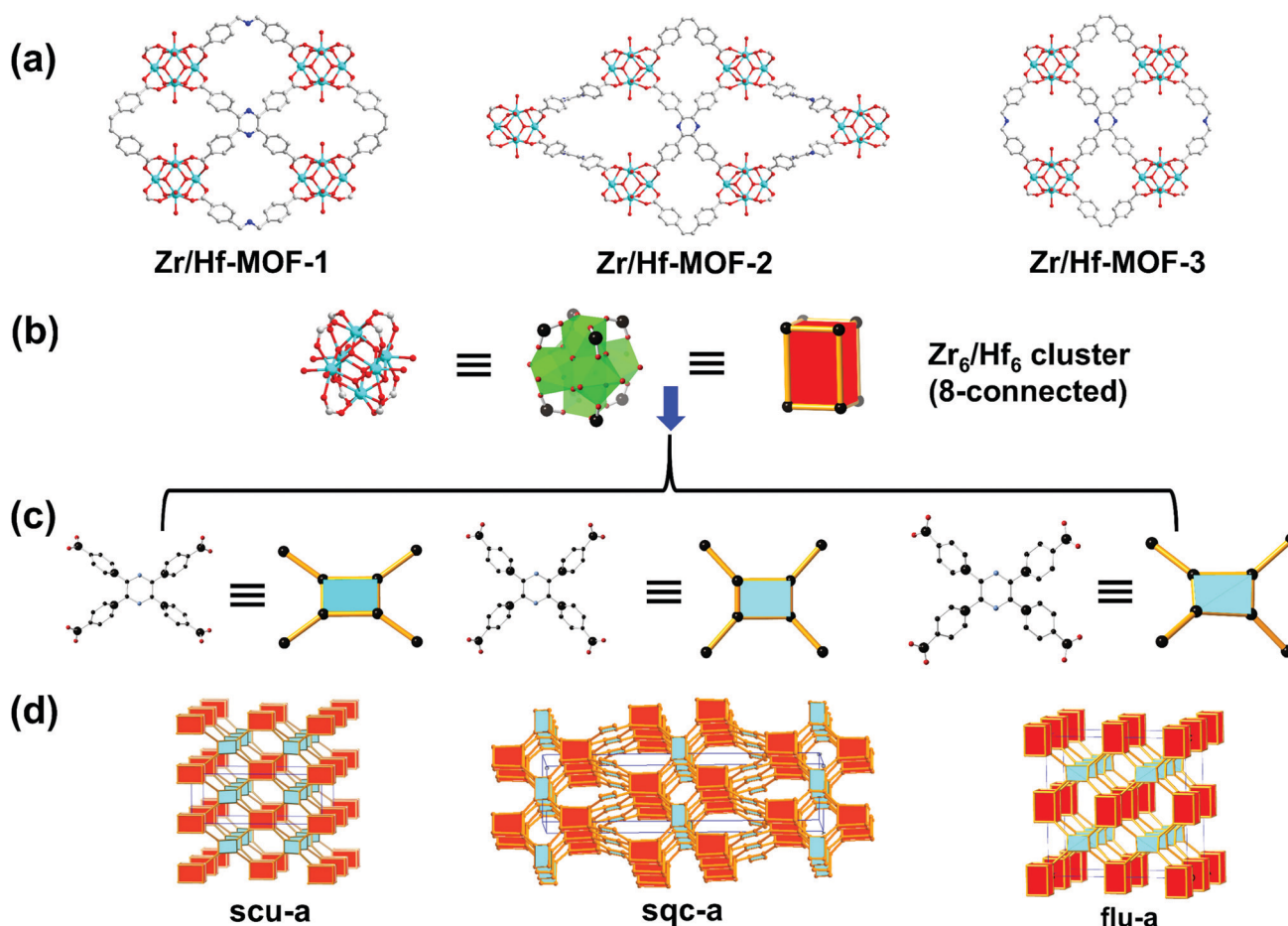

Fig. 1 (a) Crystal structures of Zr/Hf-MOF-1, Zr/Hf-MOF-2, and Zr/Hf-MOF-3 viewed along the [100] direction (colour code: C, gray; O, red; and Zr/Hf, turquoise; H atoms are omitted for clarity). (b) 8-Connected Zr_6/Hf_6 clusters with D_{4h} symmetry. (c) Conformations of the BTTB^{4-} linker in the three crystal structures and their respective 4-connected node simplification. (d) Network topologies of Zr/Hf-MOF-1, Zr/Hf-MOF-2, and Zr/Hf-MOF-3.

This journal is © The Royal Society of Chemistry 2020

J. Mater. Chem. C, 2020, **8**, 16974–16983 | **16975**

system equipped with an RA-Micro7HF-MR-DW(Cu/Mo) X-ray generator and a HyPix-6000HE Hybrid Photon Counting (HPC) X-ray detector (Rigaku, Japan, Cu Kα, graphite monochromator, λ = 1.54 Å). CCDC 2026190, 2026191, 2026199, and 2026201–2026203 contain the supplementary crystallographic data for this paper.† Thermogravimetric (TG) curves were obtained on a Mettler-Toledo (TGA/DSC) thermal analyzer from 40 °C to 800 °C with a heating rate of 10 °C min^{-1} under a nitrogen gas atmosphere (20 mL min^{-1}). Solid- and solution-state UV-Vis absorption spectra were recorded on an Agilent Cary 4000. Fourier transform infrared (FT-IR) spectra were collected on a Thermo Scientific FT-IR Nicolet iS10 spectrophotometer in the range of 4000–400 cm^{-1}. Solid- and solution-state luminescence spectra were measured on an Edinburgh FLS980 spectrofluorometer. Desktop scanning electron microscopy (DSEM) images were taken on a COXEM EM-30 PLUS System and used to examine the morphology of the crystals. Inductively coupled plasma-atomic emission spectroscopy (ICP-AES) was conducted on a Thermo Scientific iCAP 7400 ICP-OES instrument. Nitrogen gas adsorption/desorption measurements were performed on a Micromeritics ASAP 2020 Plus adsorption instrument.

2.2 Synthesis of Zr/Hf-MOFs

The scalable synthesis of Hf-MOF-2 and the recycling of mother liquid for the further synthesis of Hf-MOF-2 are described here as an example. See the ESI† for the synthesis of the other Zr/Hf-MOFs.

Synthesis of Hf-MOF-2. A mixture of HfOCl$_2$·8H$_2$O (900 mg, 2.2 mmol), H$_4$BTTB (400 mg, 0.71 mmol), and DMF/HCOOH (290 mL, 15/14, v/v) was added into a round-bottomed flask and heated up to 130 °C without stirring for 3 days. After cooling down to room temperature, polyhedron-shaped crystals were collected by filtration and washed with DMF 3 times, solvent-exchanged with acetone for 3 days, and air-dried to produce 523 mg of Hf-MOF-2 (yield 61%, based on H$_4$BTTB), which was determined as [Hf$_6$(μ_3-O)$_4$(μ_3-OH)$_4$(OH)$_4$(H$_2$O)$_4$(BTTB)$_2$]. Elemental analysis (%) for Hf-MOF-2: C, 43.09; H, 5.06; N, 4.41; found: C, 43.20; H, 5.12; N, 4.48. The experimental PXRD pattern of the bulk sample is consistent with the simulated PXRD pattern from the single-crystal X-ray data (Fig. 2b and Fig. S9, ESI†).

Synthesis of Hf-MOF-2′. In this work, we developed an economic approach for preparing Hf-MOF-2 by recycling the reaction solvents (DMF and HCOOH). After the synthesis of Hf-MOF-2, the reaction mixtures were filtered and the filtrate was used as the reaction medium for several additional batches of reactions. The same products were obtained and named Hf-MOF-2′. The DMF/HCOOH filtrate from the synthesis of Hf-MOF-2 was replenished with 900 mg of HfOCl$_2$·8H$_2$O and 400 mg of H$_4$BTTB. The resulting mixture was subjected to the same synthetic and work-up procedures as that for Hf-MOF-2. Consequently, 520 mg of microcrystalline Hf-MOF-2′ was obtained (yield: 60%, based on H$_4$BTTB). PXRD studies confirmed that Hf-MOF-2′ has the same structure as Hf-MOF-2. Notably, the DMF/HCOOH filtrate can be recycled to produce microcrystalline Hf-MOF-2′ several times with good yields (Fig. S10 and S11, ESI†).
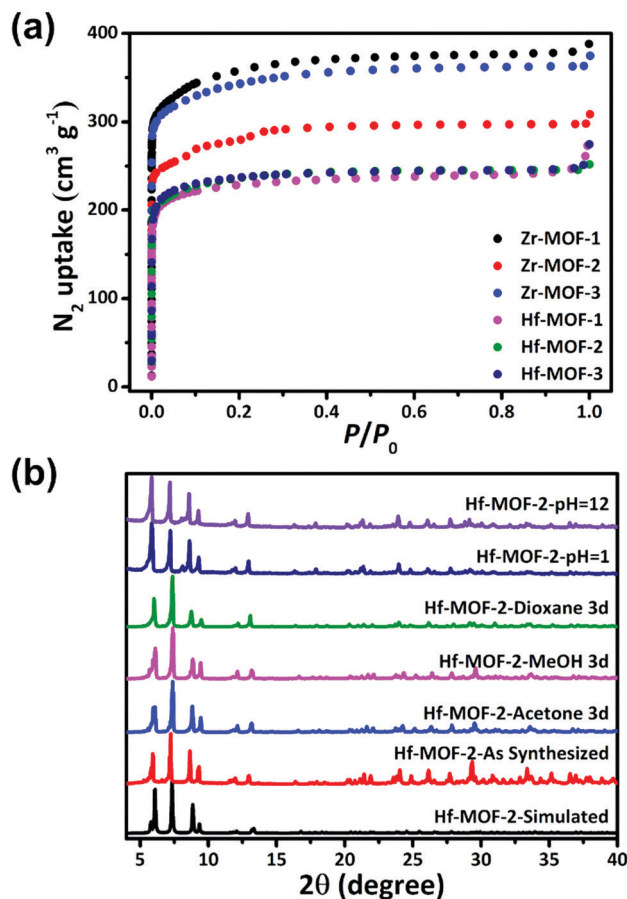

Fig. 2 (a) N$_2$ adsorption isotherms of Zr/Hf-MOF-1, -2, and -3 at 77 K; the sample was solvent-exchanged with DMF and acetone, and heated up to 100 °C for 12 h before measurement. (b) Comparison of PXRD patterns of Hf-MOF-2 and Hf-MOF-2 treated with different organic solvents, NaOH solution (pH = 13), and HCl solution (pH = 1).

Synthesis of Hf-MOF-2-Cr$_2$O$_7$$^{2-}$. The as-synthesized Hf-MOF-2 crystals (20 mg) were soaked in an aqueous solution of Cr$_2$O$_7$$^{2-}$ (5 mM) at room temperature for 4 days. Then, the crystals were collected by filtration and washed with water before further SCXRD (Fig. S2, ESI†) and PXRD (Fig. 6a) investigations.

2.3 Adsorption of Cr$_2$O$_7$$^{2-}$ from water

The experiments of Cr$_2$O$_7$$^{2-}$ adsorption from water were carried out at room temperature with desolvated Zr/Hf-MOFs. A standard curve of Cr$_2$O$_7$$^{2-}$ concentration as a function of its UV-Vis absorption intensity at λ = 350 nm was plotted (Fig. S12, ESI†), showing a good linear relationship (R^2 > 0.998). All adsorption experiments were performed in the dark on a shaker. In a typical procedure, a MOF sample (15 mg) was dispersed in 15 mL of Cr$_2$O$_7$$^{2-}$ solution. After 12 h, the MOF sample was removed by filtration, and the solution was subjected to UV-Vis absorption measurement to analyze the concentration of remaining Cr$_2$O$_7$$^{2-}$. The Cr$_2O_7$$^{2-}$ adsorption efficiency (%) was obtained using eqn (1):

$$\text{Adsorption efficiency (\%)} = \left(\frac{C_0 - C_e}{C_0}\right) \times 100\% \qquad (1)$$

16976 | J. Mater. Chem. C, 2020, 8, 16974–16983

This journal is © The Royal Society of Chemistry 2020

where C_0 and C_e (ppm) are the initial and equilibrium $Cr_2O_7^{2-}$ concentrations, respectively.

To evaluate the adsorption capacity, adsorption isotherms were measured to determine the maximum adsorption amount of each MOF. To ensure accuracy of measurement, each test was performed three times and the average value was reported. MOF samples (each 10 mg) were added to a series of aqueous solutions of different $Cr_2O_7^{2-}$ concentrations (ranging from 10 to 200 ppm, 10 mL) and left at 298 K in the dark on a shaker for 12 h. UV-Vis absorption was measured for each $Cr_2O_7^{2-}$ concentration. With the increase of $Cr_2O_7^{2-}$ concentration, $Cr_2O_7^{2-}$ adsorption increases until the maximum adsorption is reached. The adsorbed amount at equilibrium (Q_e) was obtained using eqn (2):

$$Q_e = \left(\frac{C_0 - C_e}{m}\right) \times V \qquad (2)$$

where Q_e (mg g^{-1}) is the adsorbed amount at equilibrium; C_0 and C_e (ppm) are the initial and equilibrium $Cr_2O_7^{2-}$ concentrations, respectively; V (L) represents the volume of the $Cr_2O_7^{2-}$ solution; and m (g) is the mass of the MOF. For the adsorption kinetics experiment, each MOF sample (15 mg) was dispersed in 15 mL of $Cr_2O_7^{2-}$ solution at a concentration of 100 ppm for a period of time at room temperature in the dark on a shaker. After filtration with a syringe filter, the UV-Vis absorption spectrum of the filtrate was collected to calculate the concentration according to the standard curve. The adsorbed amount was calculated using eqn (3):

$$Q_t = \left(\frac{C_0 - C_t}{m}\right) \times V \qquad (3)$$

where Q_t (mg g^{-1}) is the adsorbed amount at time t (min), C_0 is the initial concentration of $Cr_2O_7^{2-}$, C_t (mg L^{-1}) is the concentration of $Cr_2O_7^{2-}$ at time t, V (L) is the volume of the solution, and m (g) is the mass of the MOF.

2.4 Detection of $Cr_2O_7^{2-}$ in water

20 mg of the MOF was ground, dispersed in 40 mL of water, and sonicated for 20 min before use. To 2.7 mL of the above-prepared aqueous MOF suspension, 0.3 mL of $Cr_2O_7^{2-}$ aqueous solution at different concentrations was added to furnish a series of mixtures containing $Cr_2O_7^{2-}$ of controlled concentrations in the range of 0.05–300 μM. Concentration-dependent luminescence quenching of the MOF suspension by $Cr_2O_7^{2-}$ was evaluated by measuring the luminescence of the mixtures.

2.5 Selective detection of $Cr_2O_7^{2-}$ in water

To explore the influence of other anions in the luminescence sensing of $Cr_2O_7^{2-}$ in water, selective detection experiments were performed and a series of anions (Cl^-, Br^-, NO_3^-, SO_4^{2-}, PO_4^{3-}, AcO^-, ClO_4^-, MoO_4^{2-}, and WO_4^{2-}) was used. Each anion was prepared as a 0.5 mM aqueous solution, and the MOF suspension was prepared by dispersing 20 mg of the MOF sample in 40 mL of distilled water, followed by sonication for 20 min. In one experiment, the MOF suspension was mixed with one anion solution. In this case, 2.7 mL of the MOF suspension was mixed with 300 μL of an anion solution, and thus nine MOF suspensions were obtained, each containing one anion at a concentration of 0.05 mM. In another experiment, the MOF suspension was mixed with all the anion solutions. In this case, 2.7 mL of the MOF suspension was mixed with 30 μL of each anion solution. The luminescence spectra of the above-prepared suspensions were collected. After that, 30 μL of $Cr_2O_7^{2-}$ aqueous solution with a concentration of 0.5 mM was added to the suspension in the second experiment to investigate the luminescence quenching effect of $Cr_2O_7^{2-}$ in the presence of the interfering anions.

3. Results and discussion

3.1 Structural characterization

SCXRD analyses revealed that three pairs of zirconium- and hafnium-based isostructural MOFs, denoted as Zr-MOF-1 and Hf-MOF-1, Zr-MOF-2 and Hf-MOF-2, and Zr-MOF-3 and Hf-MOF-3, are (4,8)-connected 3D frameworks with **scu**, **sqc**, and **flu** topologies, respectively. The three pairs of structures are all based on the same 8-connected Zr_6/Hf_6 clusters but the 4-connected linkers are arranged in different conformations. From the perspective of connectivity, there are two crystallographically independent metal atoms (M1 and M2) in the three structures. M1 is coordinated with four O atoms from four carboxylate groups of different BTTB^{4-} linkers, two μ$_3$-O, and two μ$_3$-OH. M2 is coordinated with two O atoms from two carboxylate groups of different BTTB^{4-} linkers, two μ$_3$-O, two μ$_3$-OH, and two O atoms from the terminal H_2O/OH^- groups. Four M1 and two M2 atoms are combined with four μ$_3$-O and four μ$_3$-OH to form a $[M_6(\mu_3\text{-}O)_4(\mu_3\text{-}OH)_4]^{12+}$ cluster with D_{4h} symmetry. The $[M_6(\mu_3\text{-}O)_4(\mu_3\text{-}OH)_4]^{12+}$ clusters are further interconnected with BTTB^{4-} linkers to construct three-dimensional (3D) frameworks $[M_6(\mu_3\text{-}O)_4(\mu_3\text{-}OH)_4(OH)_4(H_2O)_4(BTTB)_2]$ (Fig. 1a). Although the three MOF structures have the same $[M_6(\mu_3\text{-}O)_4(\mu_3\text{-}OH)_4]^{12+}$ clusters, they are topologically different frameworks (Fig. 1), demonstrating that the torsional angle of the BTTB^{4-} linker significantly affects the network topology and thus leads to frameworks with different porosity.

Crystal structure of Hf-MOF-1. A structural model for microcrystalline Hf-MOF-1 was developed starting from the single crystal structure of Zr-CAU-24,[53] which was successfully simulated using the Material Studio software. Hf-MOF-1 crystallizes in the orthogonal *Cmmm* space group with unit cell parameters of $a = 21.1357$ Å, $b = 32.2067$, $c = 12.6892$ Å, and $V = 8637.68$ Å^3. The BTTB^{4-} linker is distorted with dihedral angles between the phenyl plane and the pyrazinyl plane (57.07°, 57.05°), and it can be simplified as a 4-connected node with a rectangular geometry (Fig. 1c). As a result, the 8-connected Hf$_6$ clusters and 4-connected organic linkers are assembled into a (4,8)-connected 3D framework with an **scu** topology. In the framework, there are two rhombic channels with diameters of approximately 5.3 × 10.2 Å and 6.3 × 4.1 Å. The total solvent-accessible volume of Hf-MOF-1 was calculated to be 65.5% using PLATON.

Crystal structure of Hf-MOF-2. Hf-MOF-2 crystallizes in the orthogonal *I*4$_1$/*amd* space group with unit cell parameters of $a = 14.9255(1)$ Å, $c = 61.0560(6)$ Å, and $V = 13601.48(20)$ Å^3.

This journal is © The Royal Society of Chemistry 2020

J. Mater. Chem. C, 2020, **8**, 16974–16983 | **16977**

The BTTB^{4-} linker is distorted with dihedral angles between the phenyl plane and the pyrazinyl plane (47.24°, 47.05°), and it can be simplified as a 4-connected node with a slightly different rectangular geometry (Fig. 1c). As a result, the 8-connected Hf$_6$ clusters and 4-connected organic linkers are assembled into a (4,8)-connected 3D framework with an **sqc** topology (Fig. 1). In the framework, there are two types of channels: pear-shaped and rhombic with diameters of 14.6 Å × 7.1 Å and 8.3 Å × 8.3 Å, respectively. The total solvent-accessible volume of Hf-MOF-2 was calculated to be 60.4% using PLATON.

Crystal structure of Hf-MOF-3. Hf-MOF-3 crystallizes in the orthogonal *Fmmm* space group with unit cell parameters of a = 13.3952(3) Å, b = 30.9940(4) Å, c = 30.0265(4) Å, and V = 12466.13(40) Å^3. The BTTB^{4-} linker is distorted with a dihedral angle between the phenyl plane and the pyrazinyl plane (69.23°), and it can be simplified as a 4-connected node with a quasi-tetrahedron geometry (Fig. 1c). As a result, the 8-connected Hf$_6$ clusters and 4-connected organic linkers are assembled into a (4,8)-connected 3D framework with a **flu** topology (Fig. 1). In the framework, there are two rhombic channels with diameters of 7.6 Å × 6.8 Å and 8.3 Å × 6.8 Å. The total solvent-accessible volume of Hf-MOF-3 was calculated to be 56.5% using PLATON.

Crystal structure of Hf-MOF-2-Cr$_2$O$_7^{2-}$. Hf-MOF-2-Cr$_2$O$_7^{2-}$ (Cr$_2$O$_7^{2-}$-loaded Hf-MOF-2) crystallizes in the orthogonal $I4_1/amd$ space group with unit cell parameters of a = 15.08800(10) Å, c = 60.1315(10) Å, and V = 13688.8(3) Å^3. After careful analysis of the crystal structure, it was found that two neighbouring Hf$_6$ clusters were bridged by two Cr$_2$O$_7^{2-}$ in the pear-shaped channels with two pointing terminal H$_2$O/OH$^-$ groups substituted by O atoms on Cr$_2$O$_7^{2-}$ (Fig. 6d and Fig. S2, ESI†). The total solvent-accessible volume of Hf-MOF-2-Cr$_2$O$_7^{2-}$ was calculated to be 50.2% using PLATON, which is significantly lower than that of Hf-MOF-2.

3.2 Porosity and stability

As rigid porous materials, the retention of porosity upon guest solvent removal is critical for potential applications. To assess the porosity, the as-synthesized Zr/Hf-MOFs were solvent-exchanged with DMF and acetone, and then heated up to 100 °C for 12 h. The desolvated samples were subjected to N$_2$ sorption measurement at 77 K. As shown in Fig. 2a, type I adsorption/desorption isotherms were observed for all six MOFs, indicating their microporous structures. Their BET surface areas were calculated to be around 1000 m^2 g^{-1} based on their respective adsorption isotherm branches (Table 1). Further, the calculated pore size distributions are in good agreement with the crystal structural analysis (Fig. S13, ESI†).

To evaluate the chemical stability, approximately 50 mg of the DMF and acetone solvent-exchanged Zr/Hf-MOFs was soaked in different organic solvents and different pH solutions for 12 h. PXRD patterns were collected after filtration. As shown in Fig. 2a and Fig. S14 (ESI†), after the treatments, the PXRD patterns of all the Zr/Hf-MOFs remained unchanged, indicating their exceptional chemical stability. To evaluate the thermal stability of these Zr/Hf-MOFs, thermogravimetric (TG) analyses were carried out under a N$_2$ atmosphere after 120 °C vacuum activation overnight. The TGA curves showed that all six MOFs can be stable up to 500 °C, indicating their excellent thermal stability (Fig. S15, ESI†).

3.3 Adsorption of Cr$_2$O$_7^{2-}$

The excellent chemical and thermal stability of the Zr/Hf-MOFs prompted us to investigate their practical application in the removal of Cr$_2$O$_7^{2-}$ from water. As colourless crystalline solids, one advantage of the Zr/Hf-MOFs is that the adsorption of Cr$_2$O$_7^{2-}$ can be easily distinguished by the colour change of the MOF crystals before and after being immersed in Cr$_2$O$_7^{2-}$ aqueous solution. More importantly, the restricted geometry of the organic linkers reduced their connectivity with the Zr$_6$ clusters from 12 to 8; as a result, each of the 8-connected Zr$_6$/Hf$_6$ clusters in these MOFs has four terminal OH$^-$/H$_2$O groups, which demonstrated a strong affinity towards Cr$_2$O$_7^{2-}$,[53,54] suggesting the potentially good Cr$_2$O$_7^{2-}$ capture capacity of these Zr/Hf-MOFs. As shown in Fig. 3a, Hf-MOF-2 showed fast adsorption kinetics toward Cr$_2$O$_7^{2-}$. The adsorption isotherm of Hf-MOF-2 (Fig. 3b) could be described well using the Langmuir isotherm model, and the maximum adsorption for Cr$_2$O$_7^{2-}$

Table 1 Comparison of structural parameters and Cr$_2$O$_7^{2-}$ adsorption properties of Zr/Hf-MOFs

MOFs	Topology	Unit cell volume (Å^3)	Clusters^a/ unit cell	Clusters/ MOF^b (g^{-1})	Pore size (Å)	Distance (O–O)^c (Å)	BET (m^2 g^{-1})	Q_{max}^d (mg g^{-1})	K_{sv} (M^{-1})	LOD (µM)
Zr-MOF-1 (PCN-206)[55]	**scu**	8233.6(9)	4	2.99 × 10^{20}	9.8 × 5.1 / 4.2 × 6.7	5.02, 13.53	1355.1	28	6.2 × 10^4	0.138
Zr-MOF-2 (PCN-208, HBU-18, JLU-MOF60)[55–57]	**sqc**	14004.5(3)	4	3.11 × 10^{20}	14.2 × 7.2 / 6.6 × 7.7	7.29	1015.0	149	3.5 × 10^4	0.244
Zr-MOF-3 (PCN-207)[55]	**flu**	12466.1(4)	4	3.10 × 10^{20}	7.5 × 9.3 / 6.7 × 7.7	5.94	1246.9	30	6.4 × 10^5	0.019
Hf-MOF-1	**scu**	8054.2(4)	4	2.37 × 10^{20}	5.3 × 10.2 / 6.3 × 4.1	4.90, 13.33	883.3	27	7.1 × 10^4	0.138
Hf-MOF-2	**sqc**	13601.5(2)	4	2.45 × 10^{20}	14.6 × 7.1 / 8.3 × 8.3	7.06	897.4	153	4.6 × 10^4	0.188
Hf-MOF-3	**flu**	12466.1(4)	4	2.44 × 10^{20}	7.6 × 6.8 / 8.3 × 6.8	5.56	899.0	32	4.5 × 10^5	0.013

^{a} Number of Zr$_6$/Hf$_6$–O clusters per unit cell. ^{b} Number of Zr$_6$/Hf$_6$–O clusters per gram of MOF. ^{c} Distance of opposing Zr$_6$/Hf$_6$ clusters from O to O atoms. ^{d} Maximum adsorption from the Langmuir isotherm model.

16978 | *J. Mater. Chem. C*, 2020, **8**, 16974–16983
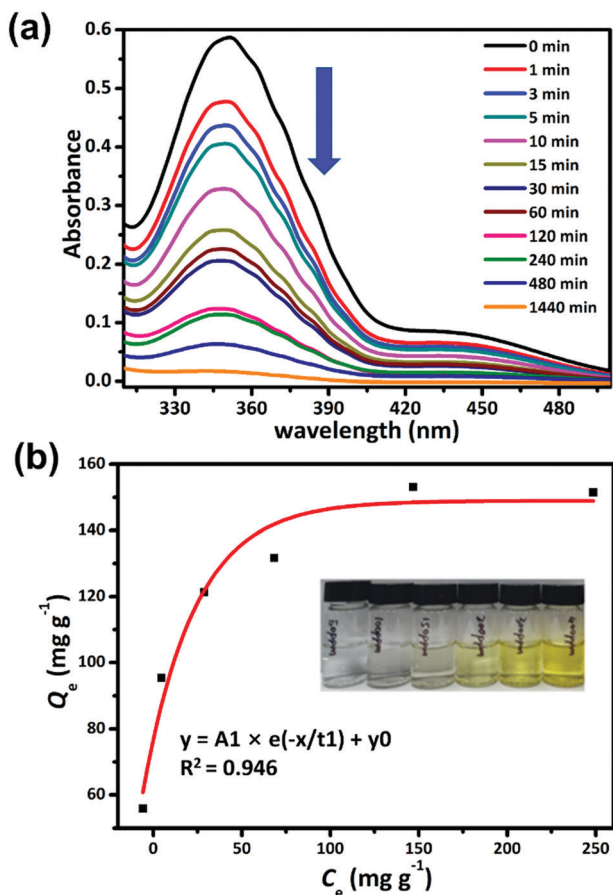
This journal is © The Royal Society of Chemistry 2020

Fig. 3 (a) Time-dependent UV-Vis absorption spectra of an aqueous solution of $Cr_2O_7^{2-}$ (50 ppm, 10 mL) upon the addition of Hf-MOF-2 (10 mg) (as described in Section 2.3). (b) Adsorption isotherm of Hf-MOF-2 for $Cr_2O_7^{2-}$ in aqueous solution (Inset: Colour change of the aqueous solutions of different $Cr_2O_7^{2-}$ concentrations after the addition of Hf-MOF-2, from left to right: 50, 100, 150, 200, 300, and 400 ppm).

could reach up to 153 mg g^{-1}, which is much higher compared to Zr/Hf-MOF-1 and Zr/Hf-MOF-2 (Table 1). The different adsorption behaviours of these Zr/Hf-MOFs may be correlated to their respective pore sizes and accessible Zr_6/Hf_6 clusters. Based on the results from inductively coupled plasma-atomic emission spectroscopy (ICP-AES, Table S3, ESI†), the metal compositions of Hf/Cr and Zr/Cr in Zr/Hf-MOF-2 are about 2/3 and 1/2, respectively. These values are larger than what is observed in the single crystal of Hf-MOF-2-$Cr_2O_7^{2-}$ (1/4). This large difference could be attributed to the single-crystal X-ray diffraction techniques, which can resolve the strongly bound guest molecules, but not the ones randomly adsorbed inside the pores. To test the recyclability, all $Cr_2O_7^{2-}$-adsorbed samples were soaked in saturated potassium nitrate solution overnight, filtered, washed with freshly distilled water, dried at 100 °C, and then reused. Taking Hf-MOF-2 as an example, almost the same adsorption performance was observed in four regeneration cycles (see Fig. S17, ESI†).

Despite having neutral skeletons, the adsorption capacities of Hf-MOF-2 and Zr-MOF-2 for $Cr_2O_7^{2-}$ surpassed that of many reported MOF materials, even the ones with cationic skeletons,

such as FIR-53[24] and 1-Br[58] (see Table S4, ESI†). Many factors could influence the adsorption capacity, such as the window/channel size, cluster density, and surface area. As shown in Table 1 and Fig. S16 (ESI†), the maximum adsorption of Zr/Hf-MOF-2 for $Cr_2O_7^{2-}$ is much higher than that of Zr/Hf-MOF-1 and -3. All six MOFs exhibit similar surface areas, indicating that the adsorption of $Cr_2O_7^{2-}$ is dominated by the strong adsorption sites, i.e. Zr_6/Hf_6 clusters. Further, the numbers of clusters per unit cell are the same for the Zr/Hf-MOFs, and the calculated number of clusters per gram of MOF is not substantially different (Table 1). Thus, we speculate that the relatively low adsorption capacities of Zr/Hf-MOF-1 and -3 are likely due to their unmatched pore sizes, which may reduce the number of clusters accessible to $Cr_2O_7^{2-}$ (Fig. S1, ESI†). In addition, the matching pore sizes in Zr/Hf-MOF-2 may play a key role in their significantly large adsorption of $Cr_2O_7^{2-}$, as evidenced by the crystal structure analyses of Zr/Hf-MOF-2-$Cr_2O_7^{2-}$ discussed in Section 3.6.

3.4 Detection of $Cr_2O_7^{2-}$

Studies have shown that the Zr/Hf-MOFs assembled from luminescent ligands have great potential as luminescence sensors.[59-61] The excellent water stability and high porosity of Zr/Hf-MOFs encouraged us to explore their application in the sensing of $Cr_2O_7^{2-}$ in water. Luminescence titrations were performed by the incremental addition of $Cr_2O_7^{2-}$ into aqueous suspensions of Zr/Hf-MOF-1, -2, and -3, and the peak intensities at 426 nm, 446 nm, and 425 nm were monitored, respectively. As expected, all the Zr/Hf-MOFs showed excellent performance in the detection of $Cr_2O_7^{2-}$. The luminescence intensity of Zr/Hf-MOFs gradually decreases with increasing $Cr_2O_7^{2-}$ amount (Fig. 4a and Fig. S18, S19, ESI†). To further evaluate the sensing performance of Zr/Hf-MOFs, the luminescence quenching efficiency was quantitatively described using the Stern–Volmer (S–V) equation in the range of 0.0 to 300 μM.[62] The quenching efficiencies of Zr/Hf-MOFs for $Cr_2O_7^{2-}$ follow the order of Hf-MOF-3 ≈ Zr-MOF-3 > Hf-MOF-2 ≈ Zr-MOF-2 > Hf-MOF-1 ≈ Zr-MOF-1. The frameworks of the six MOFs remained intact after the sensing experiments, as evidenced by PXRD analysis (Fig. S20, ESI†). The SV equation can be written as follows: $(I_0/I) = 1 + K_{sv}[M]$, where K_{sv} is the quenching constant (M^{-1}), [M] is the molar concentration of $Cr_2O_7^{2-}$, and I_0 and I are the luminescence intensities before and after the addition of $Cr_2O_7^{2-}$, respectively. As shown in Fig. 4b and c, the S–V plots for $Cr_2O_7^{2-}$ display a linear relationship at low concentrations. The limits of detection (LODs) of Zr/Hf-MOF-3 toward $Cr_2O_7^{2-}$ were calculated to be 0.013 μM and 0.019 μM (Table S4, ESI†) (LOD = $3\sigma/K_{sv}$, K_{sv}: slope, σ: standard deviation of the blank). Among them, Zr/Hf-MOF-3 demonstrates exceptionally high sensitivity in the detection of $Cr_2O_7^{2-}$ with the LODs calculated to be 0.013 μM and 0.019 μM, respectively. These values surpassed those of many reported MOF materials, such as JLU-MOF50,[63] NU-1000,[64] BUT-28[65] and BUT-39.[25] Moreover, Zr/Hf-MOF-3 can be easily regenerated by soaking in KNO$_3$ solution at 80 °C for 12 h. After three cycles of sensing experiments, both MOFs showed almost the same quenching efficiency (Fig. S17, ESI†),
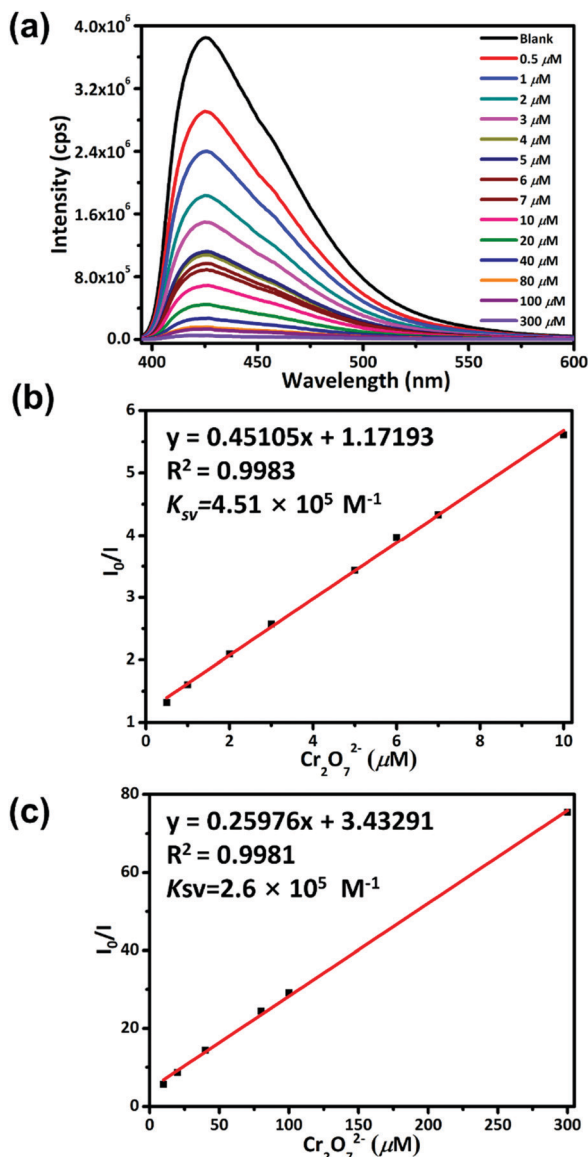
This journal is © The Royal Society of Chemistry 2020

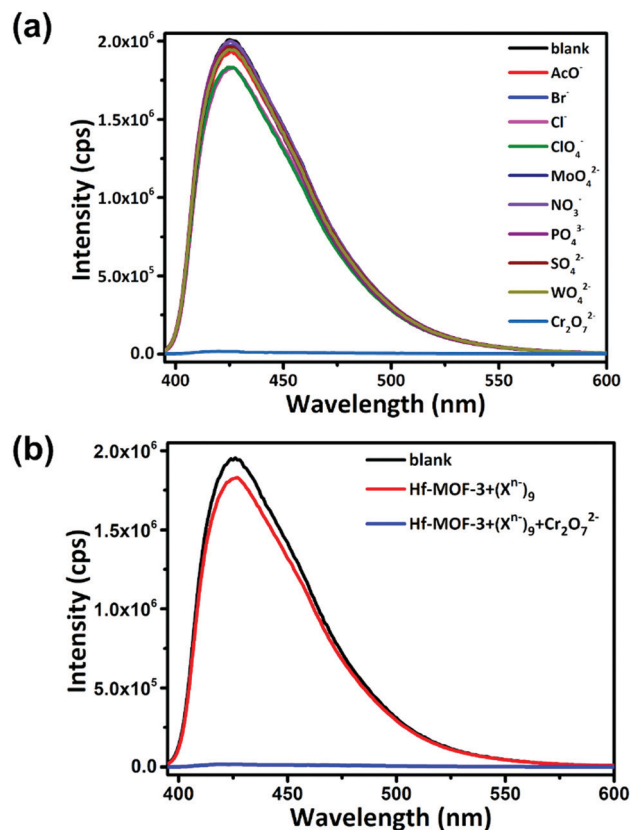J. Mater. Chem. C, 2020, 8, 16974–16983 | 16979

Fig. 5 (a) Luminescence emission spectra of aqueous suspensions of Hf-MOF-3 (20 mg/40 mL) in the presence of different anions (0.5 mM) under excitation at 380 nm. (b) Luminescence emission spectra of aqueous suspensions of Hf-MOF-3 (20 mg/20 mL) in the presence of nine potentially interfering anions (each 0.5 mM) and upon the further addition of $Cr_2O_7^{2-}$ (0.5 mM).

Further, the luminescence emissions were subsequently recorded for an aqueous suspension of Hf-MOF-3 (20 mg/40 mL) upon the addition of nine potentially competing anions (each at 0.5 mM) and the $Cr_2O_7^{2-}$ anion (0.5 mM). As shown in Fig. 5b, only a slight drift of the luminescence intensity was observed in the presence of all the competing ions, while the emission was almost completely quenched upon further addition of $Cr_2O_7^{2-}$ (0.5 mM). Therefore, it can be concluded that Hf-MOF-3 is capable of selectively detecting $Cr_2O_7^{2-}$ in aqueous solution without the interference of other common anions in wastewaters.

3.6 Detection mechanism

To better understand the luminescence quenching effect of Zr/Hf-MOFs toward $Cr_2O_7^{2-}$, we decided to look into their plausible quenching mechanisms. Take Hf-MOF-2 as an example. First, we can exclude quenching due to decomposition and/or collapse of the MOF, as evidenced by the retained PXRD pattern of Hf-MOF-2 after being soaked in $Cr_2O_7^{2-}$ aqueous solution for days (Fig. 6a). Second, as shown in Fig. S23 (ESI†), the UV-Vis spectra of the $Cr_2O_7^{2-}$ aqueous solution show broad absorption in the range of 230–500 nm, while the excitation band of Hf-MOF-2 is in the range of 280–400 nm, indicating the possibility of competitive absorption of the excitation light between Hf-MOF-2 and
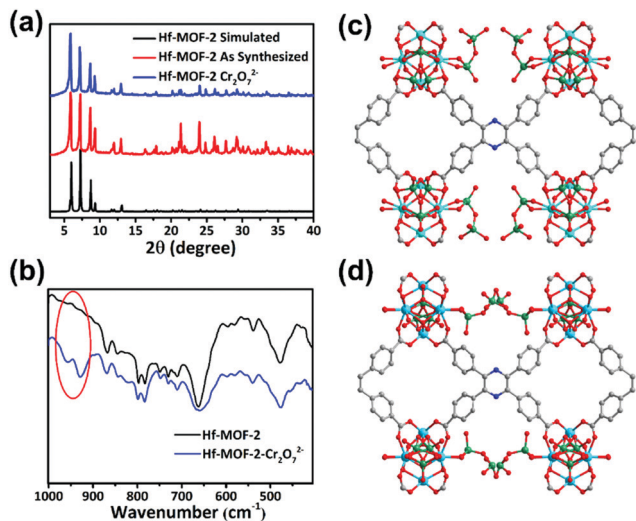

Fig. 4 (a) Concentration dependent emission spectra under excitation at 380 nm of an aqueous suspension of Hf-MOF-3 (20 mg/40 mL) upon the incremental addition of $Cr_2O_7^{2-}$ (0.5, 1, 2, 3, 4, 5, 6, 7, 8, 9, 10, 20, 40, 60, 80, 100, and 300 μM). (b) Stern–Volmer plot of I_0/I versus $Cr_2O_7^{2-}$ concentration (0.0 to 10 μM). (c) Stern–Volmer plot of I_0/I versus $Cr_2O_7^{2-}$ concentration (10–300 μM).

indicating the commendable practicability of Hf-MOF-3 and Zr-MOF-3 in the detection of $Cr_2O_7^{2-}$.

3.5 Selective detection of $Cr_2O_7^{2-}$

Besides high sensitivity, high selectivity is an equally important parameter to evaluate a probe for detection applications. The capability of selectively detecting $Cr_2O_7^{2-}$ without the interference of other anions in aqueous media is of great significance for practical applications. Taking Hf-MOF-3 as an example, it was found that the $Cr_2O_7^{2-}$ anion (0.5 mM) was able to practically quench the emission of an aqueous suspension of Hf-MOF-3 (20 mg/40 mL) with quenching efficiency as high as 96%, while other anions did not show any obvious quenching effect (Fig. 5a).

Fig. 6 (a) PXRD patterns of Hf-MOF-2 before and after adsorption of $Cr_2O_7^{2-}$ in water. (b) FT-IR spectra of Hf-MOF-2 before and after adsorption of $Cr_2O_7^{2-}$ in water. (c and d) Crystal structures of Zr-MOF-2-$Cr_2O_7^{2-}$ and Hf-MOF-2-$Cr_2O_7^{2-}$ viewed along the [010] direction using the ball-and-stick model (colour code: C, gray; O, red; and Hf, turquoise; Zr, shy blue; Cr, green; H atoms on ligands are omitted for clarity).

$Cr_2O_7^{2-}$.[66–69] Besides, it was also observed that there is an overlap between the absorption spectrum of $Cr_2O_7^{2-}$ and the emission spectrum of Hf-MOF-2, indicating the possibility of energy transfer from Hf-MOF-2 to $Cr_2O_7^{2-}$. Third, the FT-IR spectrum of Hf-MOF-2-$Cr_2O_7^{2-}$ clearly suggests interaction between the host and the guest with characteristic absorption peaks of $Cr_2O_7^{2-}$ at 929 cm^{-1} and 960 cm^{-1} (Fig. 6b),[64,70] whereas Hf-MOF-1-$Cr_2O_7^{2-}$ and Hf-MOF-3-$Cr_2O_7^{2-}$ did not clearly show such characteristic absorption peaks probably due to their low adsorption of $Cr_2O_7^{2-}$ (Fig. S24, ESI†). Finally, the terminal H_2O/OH^- groups on Zr_6/Hf_6 clusters are susceptible to replacement by $Cr_2O_7^{2-}$.[63] As shown in Fig. 6c and d, after immersing Zr/Hf-MOF-2 in $K_2Cr_2O_7$ aqueous solution for 4 days, the $Cr_2O_7^{2-}$-loaded crystal structure was successfully solved and the precise location of $Cr_2O_7^{2-}$ was pinpointed for the first time for Zr/Hf-MOFs. The results are consistent with the literature assumption of $Cr_2O_7^{2-}$ interacting with Zr_6/Hf_6 clusters by replacing the terminal H_2O/OH^- groups. In the case of Zr/Hf-MOF-2-$Cr_2O_7^{2-}$, although $Cr_2O_7^{2-}$ shows a high degree of disorder, it is clear that $Cr_2O_7^{2-}$ indeed replaced terminal H_2O/OH^- groups on the Zr_6/Hf_6 clusters, and matching pore sizes in Zr/Hf-MOF-2 allowed the two opposing clusters to accommodate two $Cr_2O_7^{2-}$ anions in the same cavity. Overall, a combined effect of competitive absorption and energy transfer seems likely to be the plausible explanation for the high luminescence quenching efficiency.[25]

4. Conclusions

In summary, we report the scalable synthesis of a series of 8-connected Zr/Hf-MOFs with different topologies using the same AIE-active ligand. Their selective detection and removal of $Cr_2O_7^{2-}$ in water were extensively studied and further correlated to their network topologies. Among them, Zr/Hf-MOF-2 exhibits a high adsorption capacity for $Cr_2O_7^{2-}$ (153 mg g^{-1} and 149 mg g^{-1}). According to the U.S. EPA standard for drinking water (100 ppb), Zr/Hf-MOF-2 appears to be a very promising candidate for the removal of $Cr_2O_7^{2-}$ from water. On the other hand, Zr/Hf-MOF-3 demonstrates exceptional sensitivity in the selective detection of $Cr_2O_7^{2-}$, and the limits of detection were calculated to be 0.013 μM and 0.019 μM, respectively. The values are comparable to those of the best-performing MOF materials reported so far. Significantly, single-crystal X-ray diffraction studies revealed the exact location and configuration of $Cr_2O_7^{2-}$ inside Zr/Hf-MOF-2. To the best of our knowledge, this is the first example of Zr/Hf-MOFs with direct evidence showing that $Cr_2O_7^{2-}$ is linked to the Zr/Hf oxide clusters within the single crystal. In conjunction with UV-Vis absorption and luminescence emission studies, the quenching mechanism was proposed to be a combined effect of competitive absorption and energy transfer. Overall, we have successfully demonstrated the detection by regulating the network topology. As versatile MOF structures, the pursuit of a suitable topology and matching pore size for targeted guests is of great significance to further improve the host–guest interaction.

Conflicts of interest

There are no conflicts to declare.

Acknowledgements

Notes and references

1 R. J. Kieber, J. D. Willey and S. D. Zvalaren, *Environ. Sci. Technol.*, 2002, **36**, 5321–5327.

2 A. Alsbaiee, B. J. Smith, L. Xiao, Y. Ling, D. E. Helbling and W. R. Dichtel, *Nature*, 2016, **529**, 190–194.

3 R. P. Schwarzenbach, B. I. Escher, K. Fenner, T. B. Hofstetter, C. A. Johnson, U. v. Gunten and B. Wehrli, *Science*, 2006, **313**, 1072–1077.

4 H. Xue, Q. Chen, F. Jiang, D. Yuan, G. Lv, L. Liang, L. Liua and M. Hong, *Chem. Sci.*, 2016, **7**, 5983–5988.

5 L. Keith and W. Telliard, *Environ. Sci. Technol.*, 1979, **13**, 416–423.

6 R. J. Kieber, J. D. Willey and S. D. Zvalaren, *Environ. Sci. Technol.*, 2002, **36**, 5321–5327.

7 J. J. Testa, M. A. Grela and M. I. Litter, *Environ. Sci. Technol.*, 2004, **38**, 1589–1594.

This journal is © The Royal Society of Chemistry 2020

J. Mater. Chem. C, 2020, **8**, 16974–16983 | **16981**

8 D. S. Sholl and R. P. Lively, *Nature*, 2016, **532**, 435–437.

9 M. Narayani and K. V. Shetty, *Crit. Rev. Environ. Sci. Technol.*, 2013, **43**, 955–1009.

10 X. Zhang, X. Li, C. Shao, J. Li, M. Zhang, P. Zhang, K. Wang, N. Lu and Y. Liu, *J. Hazard. Mater.*, 2013, **260**, 892–900.

11 M. Streat, *Ind. Eng. Chem. Res.*, 1995, **34**, 2841–2848.

12 T. H. Boyer and P. C. Singer, *Environ. Sci. Technol.*, 2008, **42**, 608–613.

13 M. Lalonde, W. Bury, O. Karagiaridi, Z. Brown, J. T. Hupp and O. K. Farha, *J. Mater. Chem. A*, 2013, **1**, 5453–5468.

14 M. Wawrzkiewicz, *Chem. Eng. J.*, 2013, **217**, 414–425.

15 H.-P. Chao, C.-K. Lee, L.-C. Juang and Y.-L. Han, *Ind. Eng. Chem. Res.*, 2013, **52**, 9843–9850.

16 L. Ai, H. Yue and J. Jiang, *Nanoscale*, 2012, **4**, 5401–5408.

17 A. Bhatnagar and M. Sillanpää, *Chem. Eng. J.*, 2010, **157**, 277–296.

18 T. Bond, E. H. Goslan, S. A. Parsons and B. Jefferson, *Water Res.*, 2010, **44**, 1645–1653.

19 D. E. Canfield, S. Zhang, A. B. Frank, X. Wang, H. Wang, J. Su, Y. Ye and R. Frei, *Nat. Commun.*, 2018, **9**, 2871.

20 W. Wu, X. Wang, C. T. Reinhard and N. J. Planavsky, *Chem. Geol.*, 2017, **456**, 98–111.

21 Z. Lv, C. Liang, J. Cui, Y. Zhang and S. Xu, *RSC Adv.*, 2015, **5**, 18213–18217.

22 X. Yuan, Y. Wang, J. Wang, C. Zhou, Q. Tang and X. Rao, *Chem. Eng. J.*, 2013, **221**, 204–213.

23 K. Xiao, F. Xu, L. Jiang, N. Duan and S. Zheng, *Chem. Eng. J.*, 2016, **283**, 1349–1356.

24 H.-R. Fu, Z.-X. Xu and J. Zhang, *Chem. Mater.*, 2014, **27**, 205–210.

25 T. He, Y. Z. Zhang, X. J. Kong, J. Yu, X. L. Lv, Y. Wu, Z. J. Guo and J. R. Li, *ACS Appl. Mater. Interfaces*, 2018, **10**, 16650–16659.

26 M. J. Kalmutzki, N. Hanikel and O. M. Yaghi, *Science*, 2018, **4**, eaat9180.

27 H. C. Zhou, J. R. Long and O. M. Yaghi, *Chem. Rev.*, 2012, **112**, 673–674.

28 H. C. Zhou and S. Kitagawa, *Chem. Soc. Rev.*, 2014, **43**, 5415–5418.

29 H. Furukawa, K. E. Cordova, M. O'Keeffe and O. M. Yaghi, *Science*, 2013, **341**, 1230444.

30 S. Yuan, L. Feng, K. Wang, J. Pang, M. Bosch, C. Lollar, Y. Sun, J. Qin, X. Yang, P. Zhang, Q. Wang, L. Zou, Y. Zhang, L. Zhang, Y. Fang, J. Li and H. C. Zhou, *Adv. Mater.*, 2018, **30**, e1704303.

31 L. Feng, J. Pang, P. She, J. L. Li, J. S. Qin, D. Y. Du and H. C. Zhou, *Adv. Mater.*, 2020, e2004414, DOI: 10.1002/adma.202004414.

32 J. R. Li, J. Sculley and H. C. Zhou, *Chem. Rev.*, 2012, **112**, 869–932.

33 W. Fan, Y. Wang, Q. Zhang, A. Kirchon, Z. Xiao, L. Zhang, F. Dai, R. Wang and D. Sun, *Chem. – Eur. J.*, 2018, **24**, 2137–2143.

34 P. L. Feng, J. J. Perry IV, S. Nikodemski, B. W. Jacobs, S. T. Meek and M. D. Allendorf, *J. Am. Chem. Soc.*, 2010, **132**, 15487–15489.

35 M. D. Allendorf, C. A. Bauer, R. K. Bhakta and R. J. Houk, *Chem. Soc. Rev.*, 2009, **38**, 1330–1352.

36 Y. Zhao, M.-Y. Wan, J.-P. Bai, H. Zeng, W. Lu and D. Li, *J. Mater. Chem. A*, 2019, **7**, 11127–11133.

37 Y. Zhao, H. Zeng, K. Wu, D. Luo, X.-W. Zhu, W. Lu and D. Li, *J. Mater. Chem. C*, 2020, **8**, 4385–4391.

38 Y. Zhao and D. Li, *J. Mater. Chem. C*, 2020, **8**, 12739–12754.

39 J. P. Bai, Y. L. Huang, M. Xie, Y. Zhao, D. Luo, Y. Y. Li, W. Lu and D. Li, *ACS Appl. Mater. Interfaces*, 2019, **11**, 38503–38509.

40 Y. L. Huang, P. L. Qiu, J. P. Bai, D. Luo, W. Lu and D. Li, *Inorg. Chem.*, 2019, **58**, 7667–7671.

41 J.-H. Wang, M. Li and D. Li, *Chem. Sci.*, 2013, **4**, 1793–1801.

42 L. Zhang, Z. Kang, X. Xin and D. Sun, *CrystEngComm*, 2016, **18**, 193–206.

43 Z. Hu, B. J. Deibert and J. Li, *Chem. Soc. Rev.*, 2014, **43**, 5815–5840.

44 C. Zou, Z. Zhang, X. Xu, Q. Gong, J. Li and C. D. Wu, *J. Am. Chem. Soc.*, 2012, **134**, 87–90.

45 J. S. Qin, S. R. Zhang, D. Y. Du, P. Shen, S. J. Bao, Y. Q. Lan and Z. M. Su, *Chem. – Eur. J.*, 2014, **20**, 5625–5630.

46 E. Quartapelle Procopio, F. Linares, C. Montoro, V. Colombo, A. Maspero, E. Barea and J. A. Navarro, *Angew. Chem., Int. Ed.*, 2010, **49**, 7308–7311.

47 J. Zheng, Z. Lu, K. Wu, G. H. Ning and D. Li, *Chem. Rev.*, 2020, **120**, 9675–9742.

48 T. Zhang and W. Lin, *Chem. Soc. Rev.*, 2014, **43**, 5982–5993.

49 J. S. Qin, S. Yuan, L. Zhang, B. Li, D. Y. Du, N. Huang, W. Guan, H. F. Drake, J. Pang, Y. Q. Lan, A. Alsalme and H. C. Zhou, *J. Am. Chem. Soc.*, 2019, **141**, 2054–2060.

50 J. H. Cavka, S. Jakobsen, U. Olsbye, N. Guillou, C. Lamberti, S. Bordiga and K. P. Lillerud, *J. Am. Chem. Soc.*, 2008, **130**, 13850–13851.

51 T. R. Cook, Y.-R. Zheng and P. J. Stang, *Chem. Rev.*, 2013, **113**, 734–777.

52 Y. Jiang, L. Sun, J. Du, Y. Liu, H. Shi, Z. Liang and J. Li, *Cryst. Growth Des.*, 2017, **17**, 2090–2096.

53 M. Lammert, H. Reinsch, C. A. Murray, M. T. Wharmby, H. Terraschke and N. Stock, *Dalton Trans.*, 2016, **45**, 18822–18826.

54 A. Yuchi and K. Matsuo, *J. Chromatogr. A*, 2005, **1082**, 208–213.

55 L. Zhang, B. Guo, H. He, X. Zhang, Y. Feng, W. Fan, J. Cao, G. Lu, Y. Chen, D. Sun and W. Huang, *Inorg. Chem.*, 2020, **59**, 695–704.

56 J.-M. Liu, J.-X. Hou, J. Liu, X. Jing, L.-J. Li and J.-L. Du, *J. Mater. Chem. C*, 2019, **7**, 11851–11857.

57 J. Liu, Y. Ye, X. Sun, B. Liu, G. Li, Z. Liang and Y. Liu, *J. Mater. Chem. A*, 2019, **7**, 16833–16841.

58 X. X. Lv, L. L. Shi, K. Li, B. L. Li and H. Y. Li, *Chem. Commun.*, 2017, **53**, 1860–1863.

59 Y. A. Li, C. W. Zhao, N. X. Zhu, Q. K. Liu, G. J. Chen, J. B. Liu, X. D. Zhao, J. P. Ma, S. Zhang and Y. B. Dong, *Chem. Commun.*, 2015, **51**, 17672–17675.

60 T. M. Suzuki, M. L. Tanco, D. A. Pacheco Tanaka, H. Matsunaga and T. Yokoyama, *Sep. Sci. Technol.*, 2006, **36**, 103–111.

61 W. Zhang, H. Huang, D. Liu, Q. Yang, Y. Xiao, Q. Ma and C. Zhong, *Microporous Mesoporous Mater.*, 2013, **171**, 118–124.

62 A. Das and S. Biswas, *Sens. Actuators, B*, 2017, **250**, 121–131.

63 X. Sun, S. Yao, C. Yu, G. Li, C. Liu, Q. Huo and Y. Liu, *J. Mater. Chem. A*, 2018, **6**, 6363–6369.

64 Z. J. Lin, H. Q. Zheng, H. Y. Zheng, L. P. Lin, Q. Xin and R. Cao, *Inorg. Chem.*, 2017, **56**, 14178–14188.

65 M. M. Xu, X. J. Kong, T. He, X. Q. Wu, L. H. Xie and J. R. Li, *Inorg. Chem.*, 2018, **57**, 14260–14268.

66 R. Lv, J. Wang, Y. Zhang, H. Li, L. Yang, S. Liao, W. Gu and X. Liu, *J. Mater. Chem. A*, 2016, **4**, 15494–15500.

67 H. He, Y. Song, F. Sun, Z. Bian, L. Gao and G. Zhu, *J. Mater. Chem. A*, 2015, **3**, 16598–16603.

68 W. Liu, Y. Wang, Z. Bai, Y. Li, Y. Wang, L. Chen, L. Xu, J. Diwu, Z. Chai and S. Wang, *ACS Appl. Mater. Interfaces*, 2017, **9**, 16448–16457.

69 Y. Lin, X. Zhang, W. Chen, W. Shi and P. Cheng, *Inorg. Chem.*, 2017, **56**, 11768–11778.

70 X. Li, H. Xu, F. Kong and R. Wang, *Angew. Chem., Int. Ed.*, 2013, **52**, 13769–13773.

This journal is © The Royal Society of Chemistry 2020

J. Mater. Chem. C, 2020, **8**, 16974–16983 | **16983**